

Supporting Information for:

KBaTeBiO₆: a lead-free, inorganic double perovskite semiconductor

for photovoltaic applications

Arashdeep Singh Thind,[†] Shaline Kavadiya,[‡] Mojgan Kouhnavard,[‡] Robin Wheelus,[†] Sung Beom Cho,^{§,¶} Liang-Yi Lin,[‡] Clayton Kacica,[‡] Hemant Kumar Mulmudi,^{||} Kinga A. Unocic,[⊥] Albina Y. Borisevich,[⊥] Ghanshyam Pilania,[#] Pratim Biswas,[‡] and Rohan Mishra^{§,†}

[†]Institute of Materials Science & Engineering, [‡]Department of Energy, Environmental and Chemical Engineering, [§]Department of Mechanical Engineering & Materials Science, Washington University in St. Louis, One Brookings Drive, St. Louis, MO 63130, USA

^{||}Research School of Electrical, Energy and Materials Engineering, College of Engineering and Computer Science, Australian National University, Canberra 2601, Australia

[⊥]Center for Nanophase Materials Sciences, Oak Ridge National Laboratory, Oak Ridge, TN 37831, USA

[#]Materials Science and Technology Division, Los Alamos National Laboratory, Los Alamos, NM 87545, USA

[¶]Current address: Virtual Engineering Center, Korea Institute of Ceramic Engineering and Technology, Jinju 52851, Republic of Korea

Calculation of formation enthalpy:

The method for the determination of the most probable reaction pathway is based on an evaluation of the convex hull in multi-dimensional phase space and subsequent minimization of the free energy of the multicomponent reactants, assuming a reversible chemical reaction. For any hypothetical chemistry, the multi-component reactants and their coefficients are generated using the grand canonical linear programming (GCLP) approach implemented within OQMD.¹⁻² The formation enthalpy and thermodynamic stability of a hypothetical double perovskite can be then evaluated from the DFT total energy of the double perovskite and the combined total energy of the reactants. For instance, Eq. S1 shows the reaction pathway for KBaTeBiO₆, as evaluated by OQMD. The formation enthalpy of this compound ($\Delta H_f(\text{KBaTeBiO}_6)$) is calculated using Eq. S2, where $E(\text{KBaTeBiO}_6)$ is the DFT total energy/f.u. of KBaTeBiO₆, while $E(\text{K}_2\text{TeO}_3)$, $E(\text{Bi}_2\text{O}_3)$, $E(\text{KBiO}_3)$ and $E(\text{Ba}_3\text{Te}_2\text{O}_9)$ are DFT total energies/f.u. of the reactants obtained from OQMD. This methodology for calculating formation enthalpy using multi-component reactants is more accurate than using elemental energies as the reference point. However, it should be noted that the estimation of the optimal reactants in a reaction pathway is limited to the structures calculated within the OQMD database.



$$\Delta H_f(\text{KBaTeBiO}_6) = E(\text{KBaTeBiO}_6) - [E(\text{K}_2\text{TeO}_3) - E(\text{Bi}_2\text{O}_3) - E(\text{KBiO}_3) - E(\text{Ba}_3\text{Te}_2\text{O}_9)]/3 \quad \text{Eq. S2}$$

Octahedral tilts in double perovskites:

The perovskite framework can accommodate a variety of cations with different oxidation states and ionic radii for both type of cations for a fixed choice of anion at the *X*-site. This is achieved through cooperative tiltings of the BX_6 octahedra.³ These tilts allow for the optimization of the coordination environment of the *A*-site cations, where the extent and type of tilting are dependent on the relative size of the cubo-octahedral cavities and the size of the *A*-site cation. The octahedral tilts and their effects on the space group symmetry have been studied extensively for the double perovskite structure.⁴⁻⁶ These results are summarized in Table S1.

Table S1. List of space group symmetry and the corresponding octahedral tilt patterns for the $A'A''B'B''O_6$ and $A_2B'B''O_6$ systems

$A'A''B'B''O_6$			$A_2B'B''O_6$		
index	space group	tilt system	index	space group	tilt system
2	$P\bar{1}$	$a^-b^-c^-$	2	$P\bar{1}$	$a^-b^-c^-$
4	$P2_1$	$a^-a^-c^+$	12	$C2/m$	$a^0b^-b^-$
5	$C2$	$a^-b^0c^+$	14	$P2_1/c$	$a^+b^-b^-$
11	$P2_1/m$	$a^-a^-c^0$	15	$C2/c$	$a^0b^+c^-$
12	$C2/m$	$a^0b^-c^0$	48	$Pnnn$	$a^+b^+c^+$
13	$P2/c$	$a^+b^-c^0$	86	$P4_2/n$	$a^+a^+c^-$
16	$P222$	$a^+b^+c^+$	87	$I4/m$	$a^0a^0c^-$
49	$Pccm$	$a^+b^0c^0$	128	$P4/mnc$	$a^0a^0c^+$
81	$P4$	$a^+a^+c^-$	134	$P4_2/nm$	$a^0b^+b^+$
85	$P4/n$	$a^0a^0c^-$	148	$R\bar{3}$	$a^-a^-a^-$
90	$P42_12$	$a^0a^0c^+$	201	$Pn\bar{3}$	$a^+a^+a^+$
111	$P42m$	$a^+a^+c^0$	225	$Fm\bar{3}m$	$a^0a^0a^0$
129	$P4/nmm$	$a^0a^0c^0$			

Electronic structure of SrBaVBiO₆:

Most of the screened double perovskite oxides exhibit wide band gaps with flat electronic bands. As shown in Figure S1, SrBaVBiO₆ exhibits flat electronic bands, with an indirect PBE band gap of 1.61 eV and scaled HSE+SOC (approximated as described in main text) band gap of 2.18 eV. The electronic band characteristics are expected to be similar for PBE and HSE+SOC calculations. These flat bands are also observed for other compounds such as RbSrNbBiO₆ and KSrMoBiO₆, which have a transition metal cation at the *B*-site. The reason for the indirect band gap and flat bands in case of double perovskite oxides can be understood by analyzing the DOS plot (Figure S1). In SrBaVBiO₆, the valence band is predominantly made up of O-2*p*, O-2*s*, V-3*p* with a small contribution from Bi-6*p* and V-3*d* states respectively. The contribution of the *d*-states at the valence band edge is responsible for the indirect nature of the band gap for SrBaVBiO₆. This is similar to the effect of Ag-4*d* states in case of Cs₂AgBiBr₆ and Cs₂AgBiCl₆.⁷ The conduction band edge is predominantly made up of O-2*p* and V-3*d*. As compared to KBaTeBiO₆ (Figure 3b), the contribution of the V-3*d* states contribute significantly more towards band edges than the Te-4*d* states. This increased contribution of the V-3*d* states in SrBaVBiO₆ leads to the flattening of the electronic bands at both the conduction and valence band edges. As a result, for most double perovskite oxides with transition metal cations at the *B*-site, the significantly high contribution of *d* states at the conduction band edge, renders the electronic transport non-ideal for photovoltaic action. From DOS analysis, we conclude that while designing novel perovskite photovoltaics transition metal cations are not ideal choices for the *B*-site cations.

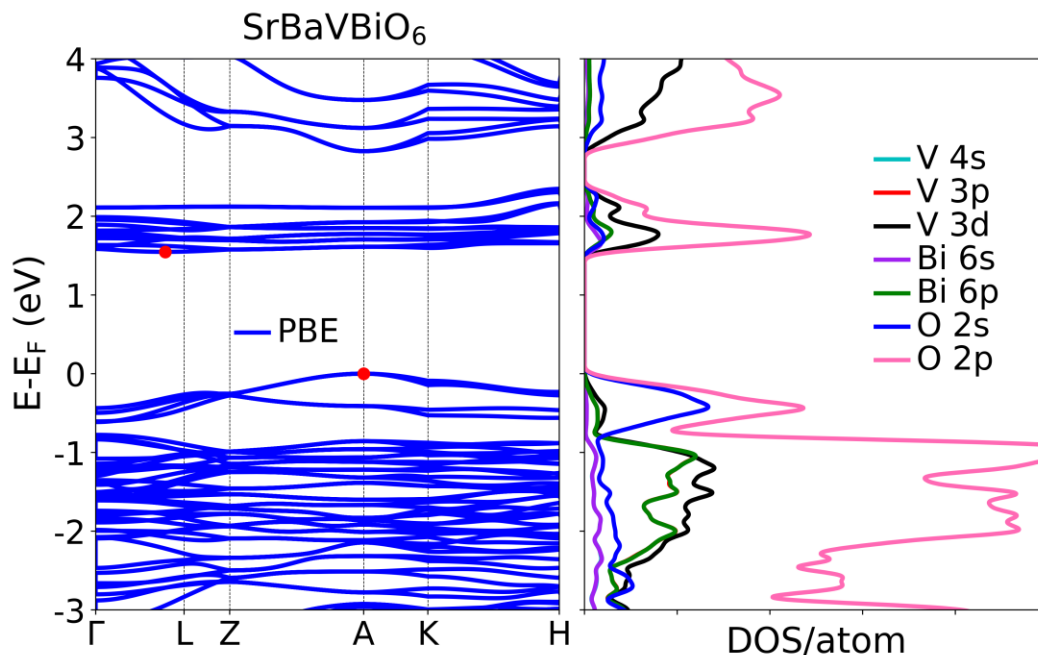


Figure S1. Calculated band structure (left) and DOS (right) for the cubic SrBaVBiO₆ calculated using PBE.

Chemical bonding analysis for KBaTeBiO₆:

As shown in Figure S2, we find that the valence band edge is predominantly composed of (Bi-6s)–(O-2p) antibonding interactions while the conduction band edge is composed of (Bi-6p)–(O-2s), (Te-5s)–(O-2p) and (Te-5s)–(O-2s) antibonding interactions. The contribution of O-2p states is significantly lower in COHP plot than in the DOS plot near the valence band edge, which is due to a large amount of non-bonding O-2p states. The chemical bonding analysis was performed using plane wave based crystal orbital Hamilton population (COHP) analysis.⁸⁻¹¹

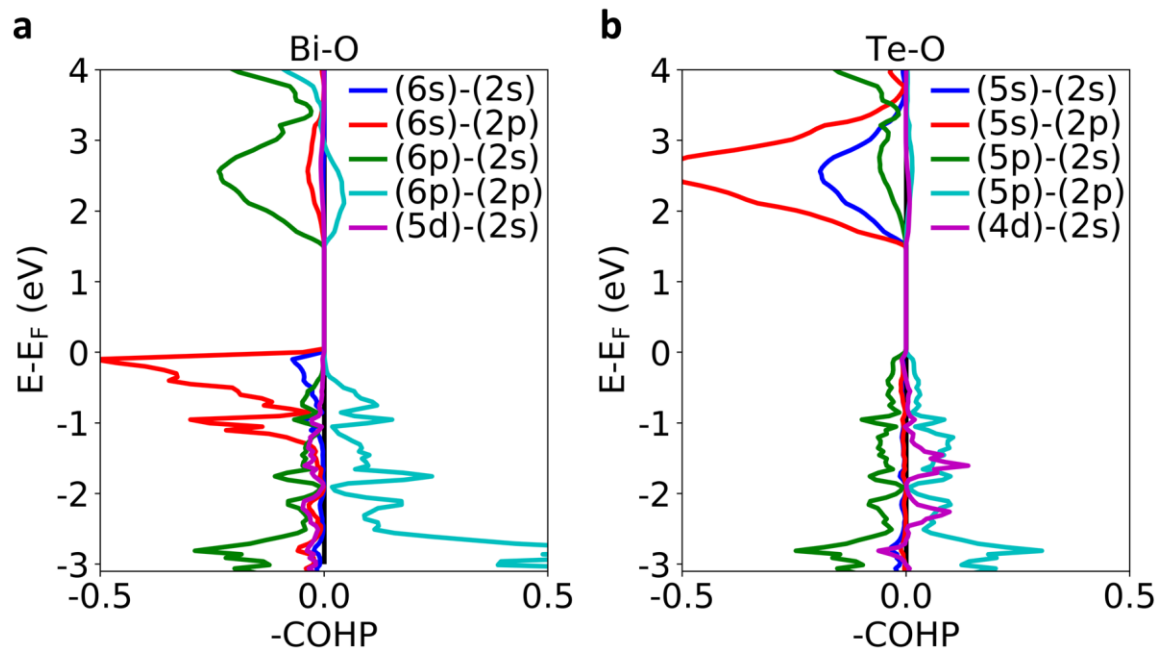


Figure S2. Crystal orbital Hamilton population (COHP) bonding analysis of KBaTeBiO_6 for (a) Bi-O and (b) Te-O bonds. Positive values indicate bonding character while negative values indicate antibonding character.

Calculated absorption spectra for KBaTeBiO_6 :

The absorption spectra of KBaTeBiO_6 , calculated using HSE06+SOC, is provided in Figure S3. It can be clearly seen that there is a small absorption onset around the indirect band gap followed by a large photon absorption onset that occurs at a larger value than the indirect band gap and is almost equal to the direct band gap value. The presence of an indirect band gap implies the use of a thicker layer of absorber material for large photoconversion efficiency. We also show the calculated absorption spectrum of $\text{Cs}_2\text{AgBiBr}_6$ in Figure S3 for comparison, which shows similar characteristics to that of KBaTeBiO_6 . The comparison of the absorption spectra of KBaTeBiO_6 and $\text{Cs}_2\text{AgBiBr}_6$ further illustrates the expected similarity in the photovoltaic performance of both

materials. For calculating the absorption spectra, the total number of bands was tripled with respect to the DFT default to accommodate sufficient empty conduction bands.

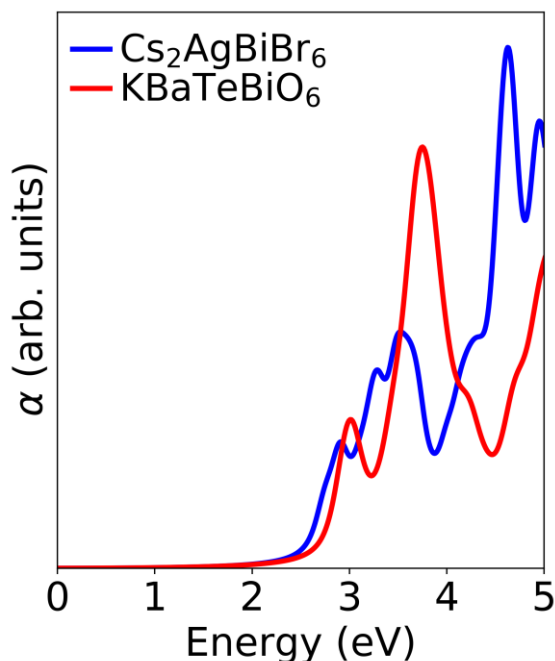


Figure S3. Comparison of the absorption spectra of cubic $\text{Cs}_2\text{AgBiBr}_6$ and KBaTeBiO_6 calculated using HSE06 functional with spin-orbit coupling effects (SOC).

Thermogravimetric analysis:

Thermogravimetric analysis (Figure S4) on the mixed precursor powder shows the mass change in the temperature range of 200 – 650 °C, consisting of initial slow mass loss (below 400 °C) and rapid mass loss (above 400 °C). The weight loss below 200 °C is generally caused by the desorption of physically and/or chemically adsorbed water in the sample, while the loss at higher temperatures results from the decomposition of barium, potassium, bismuth nitrates, telluric acid (thermal decomposition temperature in the range of 400-650 °C).¹²⁻¹³ Therefore, based on the TGA

profile, we choose the two temperatures, 500 °C and 600 °C, to transform the mixed precursors to the perovskite with desired stoichiometry.

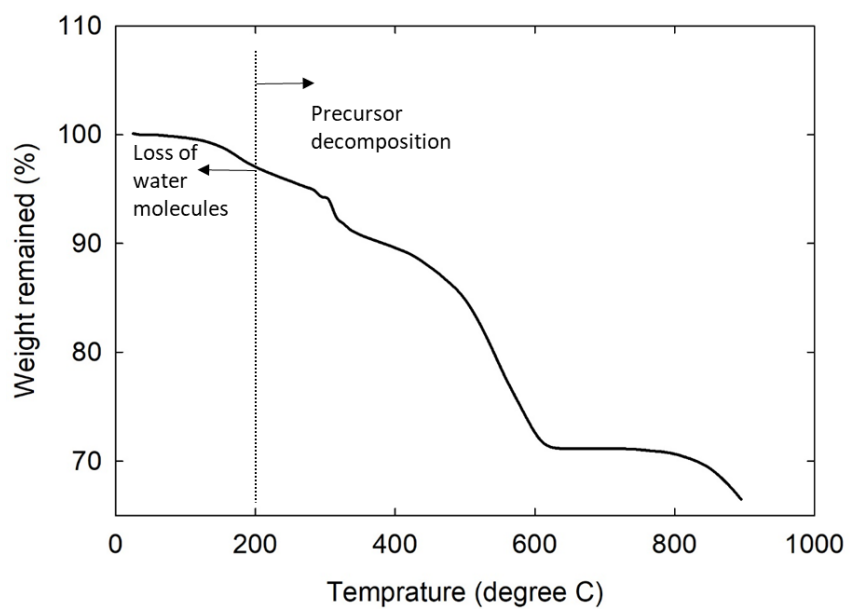


Figure S4. TGA profile of the dried precursor.

Stability of as-synthesized KBaTeBiO_6 powder:

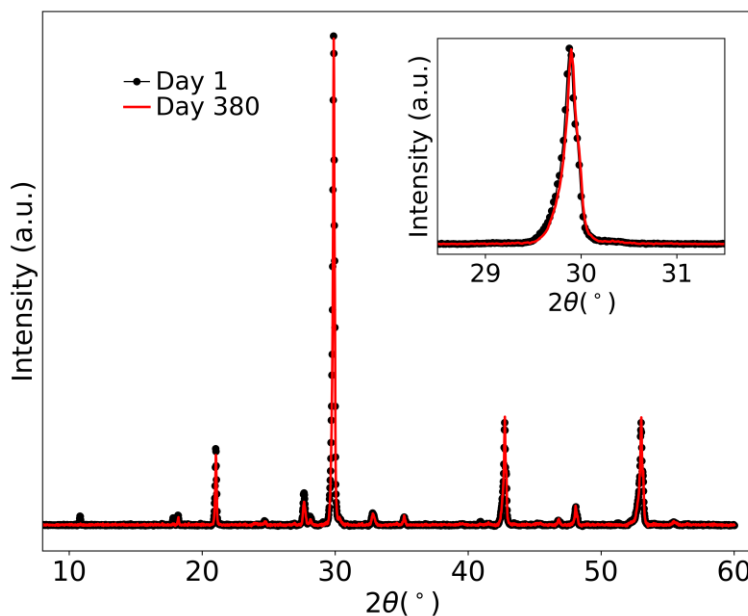


Figure S5. Overlaid XRD patterns of freshly prepared (black) KBaTeBiO_6 and after storing under ambient conditions for 380 days (red).

STEM-EDS analysis:

Table S2. Composition analysis for various EDS datasets for the KBaTeBiO_6 system.

S.	K atomic %	Ba atomic %	Te atomic %	Bi atomic %
1	10.91	35.44	28.00	25.65
2	12.57	33.32	26.71	27.40
3	11.45	30.75	24.44	33.36
4	11.55	30.28	25.29	32.88
5	10.76	37.90	26.70	24.64
6	10.83	30.79	26.09	32.29
Average	11.35 ± 0.69	33.08 ± 3.08	26.2 ± 1.24	29.37 ± 3.92

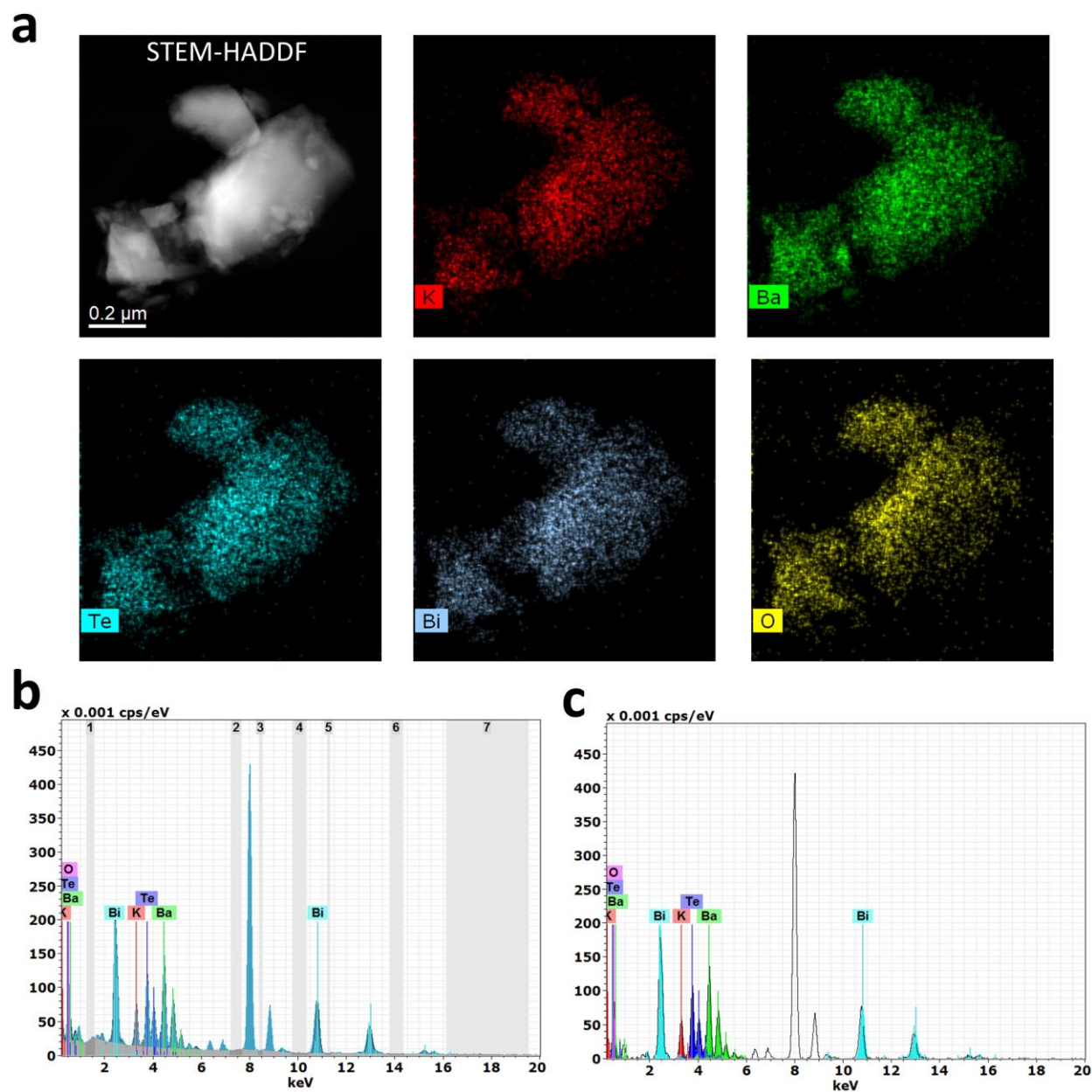


Figure S6. (a) HAADF image and elemental EDS maps of representative KBaTeBiO_6 particles. (b) Integrated raw spectra of the region shown in (a), showing background windows (grey) for each peak. (c) The deconvoluted integrated spectrum obtained after removing the background spectrum (as shown in (b)). This dataset corresponds to S. No. 2 in Table S2.

STEM-EELS analysis:

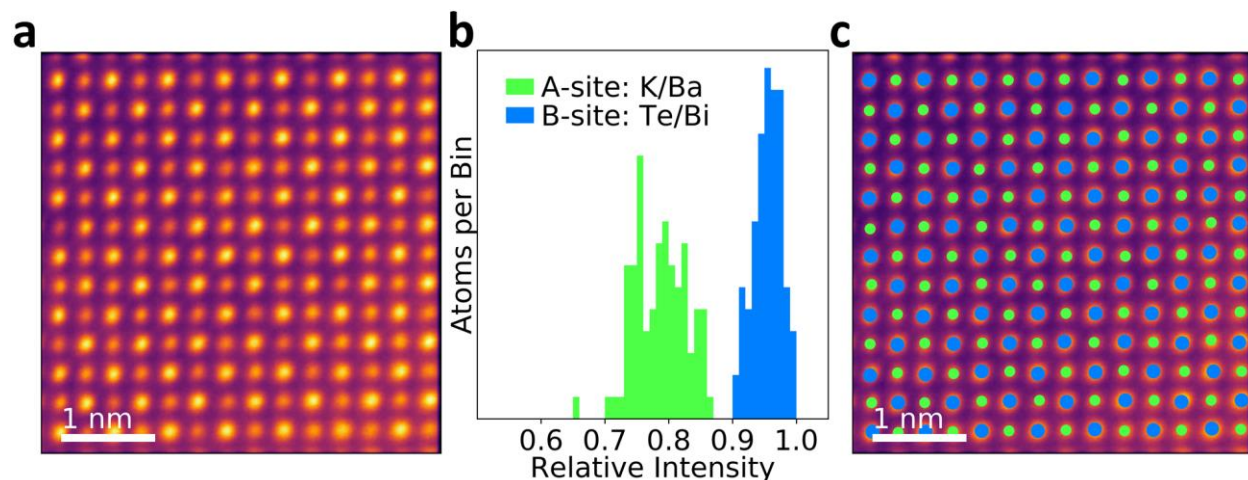


Figure S7. (a) Atomic resolution HAADF image showing the (001) projection of KBaTeBiO_6 lattice. (b) Intensity profile of HAADF image shown in (a). (c) HAADF image with labeled atomic columns according to the intensity profile shown in (b).

Figure S7a shows an atomic resolution HAADF (same as the HAADF image shown in Figure 4b (bottom)) image showing the (001) projection of the KBaTeBiO_6 perovskite structure. Since the intensity at every point in a HAADF image is approximately proportional to the squared atomic number ($\sim Z^2$) of the atomic column,¹⁴ each atomic column can thus be labeled. Figure S7b shows the histogram plot of intensities collected from the image in Figure S7a. The histogram plot clearly shows two types of profiles, where the lower intensity profile (green) corresponds to the atomic columns with lower Z (A-site: K/Ba) while the higher intensity profile (blue) corresponds to the atomic column with higher Z (B-site Te/Bi). Figure S8c shows the HAADF image with labeled atomic columns according to the intensity profiles in Figure S8b. The labeled HAADF image clearly shows the (001) projection of the perovskite phase where all the B -site cations have four in-plane A -site nearest neighbors.

To discern the chemical composition of the KBaTeBiO_6 powder, we have further performed EELS analysis. Figure S8 shows the HAADF image of the sample with the highlighted region (white box) showing the area chosen for EELS data acquisition. We have performed principal component analysis (PCA), to remove random noise, such that each data set is described predominantly by the EELS edges of the respective elements.¹⁵⁻¹⁶ A Scree plot showing the contribution of each component towards variance is shown in Figure S8b. We have selected the first five principal components ($n=5$) for subsequent elemental maps. We observe absorption onsets for K *L*, Ba *M* and O *K* edges at 296 eV (294 eV), 770 eV (781 eV) and 525 eV (532 eV) respectively, where values in the parenthesis correspond to the ionization edges for the pure elements. While Te *M* edge shows a delayed absorption onset at 580 eV (572 eV). The chemical shifts induced in the EELS edges of each element with respect to its pure elemental state is caused by changes in the chemical bonding environment as a result of the formation of KBaTeBiO_6 . We couldn't simultaneously acquire a high-quality Bi core-loss edge, as it appears at a significantly higher energy of 2580 eV, which is beyond the number of channels of the spectrometer. We have fitted a power law background model prior to every EELS edge and subsequently integrated each edge to generate chemical maps for each element as shown in Figure S8c, confirming the presence of these elements. Figure S8d shows the extracted EELS signal for each element from the region highlighted (white box) in their respective chemical maps.

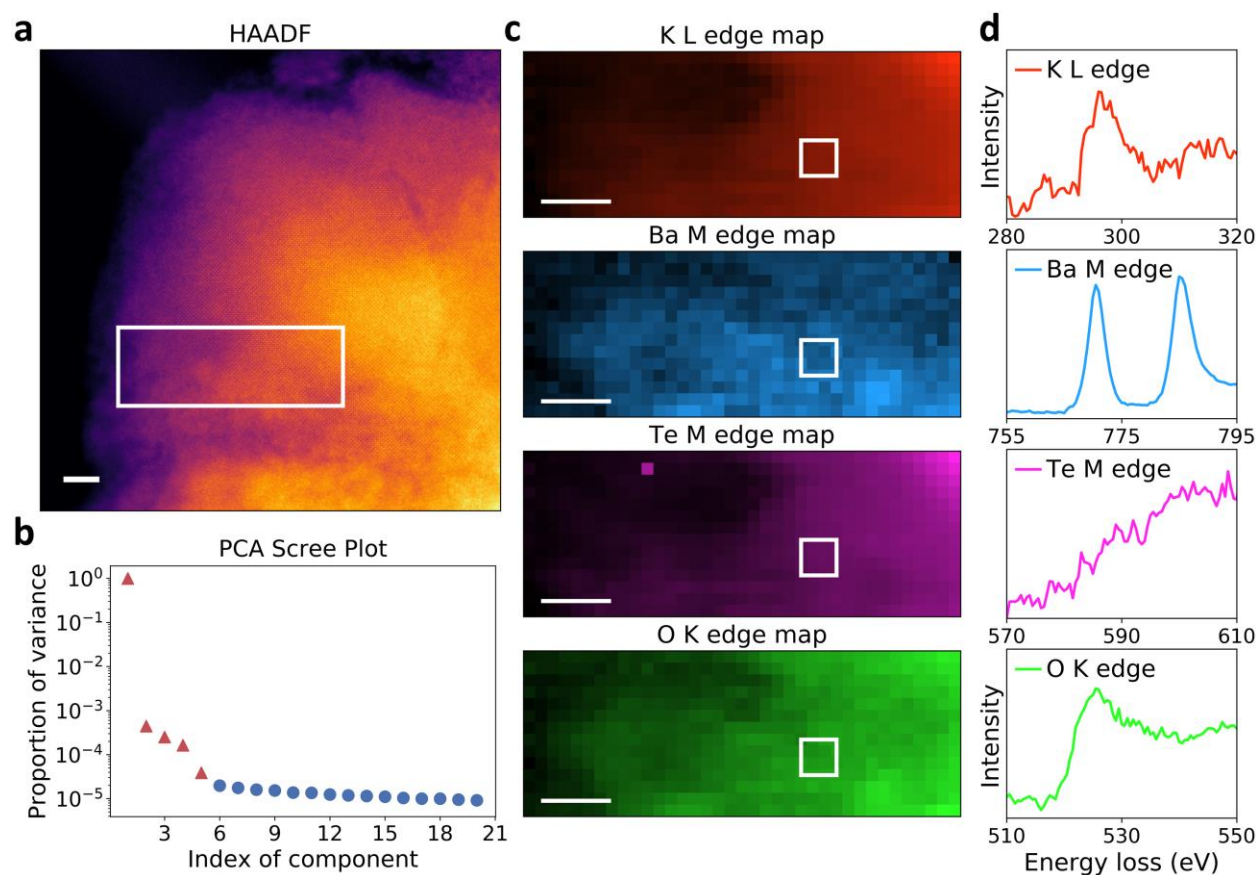


Figure S8. (a) HAADF image showing the area chosen (white box) for EELS data acquisition. (b) PCA Scree plot showing the principal components ($n \leq 5$) and random noise components ($n \geq 6$). (c) Integrated K-L, Ba-M, Te-M and O-K edge maps generated after PCA. (d) Extracted EELS signal from the area highlighted in (c) (white boxes). Scale bars in (a,c) correspond to 5 nm.

Effect of cation non-stoichiometry on electronic structure:

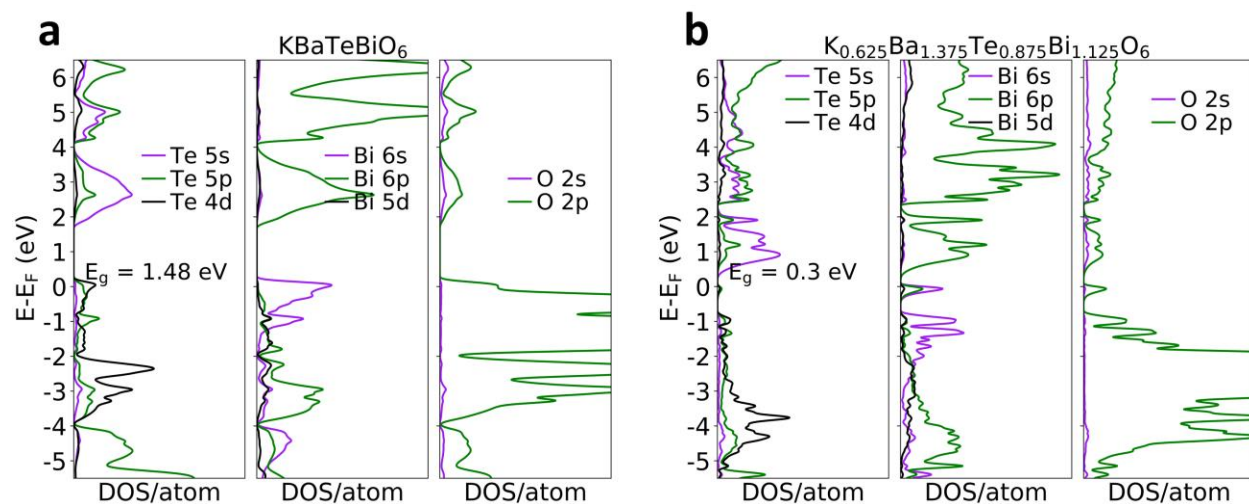


Figure S9. Calculated DOS at PBE level of (a) stoichiometric double perovskite composition of KBaTeBiO_6 and (b) non-stoichiometric composition of $\text{K}_{0.625}\text{Ba}_{1.375}\text{Te}_{0.875}\text{Bi}_{1.125}\text{O}_6$.

Device architecture and performance:

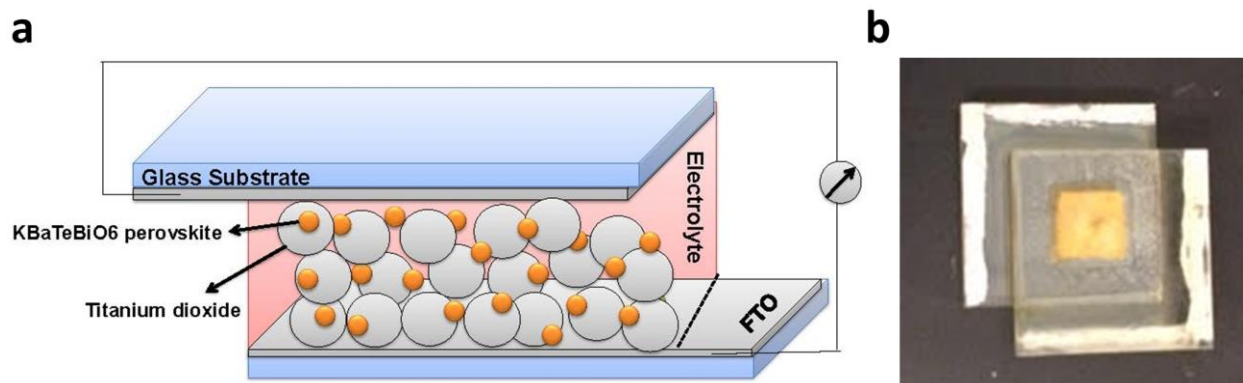


Figure S10. (a) Schematic illustrating the architecture of the regenerative host-scaffold photoelectrochemical (PEC) solar cell fabricated in this work. (b) Image of one of the fabricated cells.

Table S3. Photovoltaic parameters of devices fabricated without and with binder in the KBaTeBiO₆ solution.

Without binder				
Cell number	J_{sc} (mA/cm ²)	V_{oc} (V)	FF	Efficiency (%)
1	0.08	0.568	0.54	0.048
2	0.09	0.545	0.58	0.057
3	0.08	0.353	0.42	0.025
4	0.04	0.67	0.53	0.028
5	0.04	0.68	0.56	0.031
With binder				
1	0.066	0.29	0.405	0.016
2	0.06	0.32	0.401	0.015
3	0.01	0.34	0.305	0.002
4	0.013	0.17	0.26	0.001
5	0.072	0.314	0.38	0.017
6	0.09	0.3	0.31	0.017

Perovskite oxide-based photovoltaic devices:

A summary of performance of oxide-based ferroelectric photovoltaics is provided in Table S3. The open circuit voltage (V_{oc}) for our KBaTeBiO_6 nanoparticle-based PEC solar cells without binder is comparable to that reported for many other oxide thin films-based cells. The short circuit current density (J_{sc}), however, is lower for our PEC solar cell than for the reported oxide-based devices. The current density and efficiency of our PEC solar cells can further be improved by optimizing the material composition and microstructure, and the electrode layers in the cell.

Table S4. Summary of photovoltaic performance of oxide-based devices from literature.

#	Compound	Efficiency (%)	V_{oc} (V)	J_{sc} (mA/cm^2)	Reference
1.	FTO/ TiO_2 / KBaTeBiO_6 /iodide-triiodide/Pt	0.057	0.545	0.09	This work
2.	$\text{Bi}_2\text{FeCrO}_6$	8.1	0.84	20.6	¹⁷
3.	$\text{Pb}(\text{Zr},\text{Ti})\text{O}_3$	0.57	0.6	4.8	Cao, et al. ¹⁸
4.	$(\text{Pb}_{0.97}\text{La}_{0.03})(\text{Zr}_{0.52}\text{Ti}_{0.48})\text{O}_3$	0.28	0.7	0.0008	Qin, et al. ¹⁹
5.	Pr-doped BiFeO_3	0.5	0.21	-	Gopal Khan, et al. ²⁰
6.	$\text{BiFeO}_3/\text{Nb-SrTiO}_3$	0.03	0.15	6	Qu, et al. ²¹

Additional References:

1. Kirklin, S.; Saal, J. E.; Meredig, B.; Thompson, A.; Doak, J. W.; Aykol, M.; Rühl, S.; Wolverton, C., The Open Quantum Materials Database (OQMD): assessing the accuracy of DFT formation energies. *NPJ Comput. Mater.* **2015**, *1*, 15010.
2. Saal, J. E.; Kirklin, S.; Aykol, M.; Meredig, B.; Wolverton, C., Materials Design and Discovery with High-Throughput Density Functional Theory: The Open Quantum Materials Database (OQMD). *JOM* **2013**, *65* (11), 1501-1509.
3. Woodward, P. M., Octahedral Tilting in Perovskites. I. Geometrical Considerations. *Acta Crystallogr., Sect. B: Struct. Crystallogr. Cryst. Chem.* **1997**, *53* (1), 32-43.
4. Knapp, M. C.; Woodward, P. M., A-site cation ordering in $AA'BB'O_6$ perovskites. *J. Solid State Chem.* **2006**, *179* (4), 1076-1085.
5. Howard, C. J.; Stokes, H. T., Structures and phase transitions in perovskites - a group-theoretical approach. *Acta Crystallogr., Sect. A: Found. Adv.* **2005**, *61* (1), 93-111.
6. Howard, C. J.; Kennedy, B. J.; Woodward, P. M., Ordered double perovskites - a group-theoretical analysis. *Acta Crystallogr., Sect. B: Struct. Sci., Cryst. Eng. Mater.* **2003**, *59*, 463-471.
7. McClure, E. T.; Ball, M. R.; Windl, W.; Woodward, P. M., Cs_2AgBiX_6 (X = Br, Cl): New Visible Light Absorbing, Lead-Free Halide Perovskite Semiconductors. *Chem. Mater.* **2016**, *28* (5), 1348-1354.
8. Dronskowski, R.; Bloechl, P. E., Crystal orbital Hamilton populations (COHP): energy-resolved visualization of chemical bonding in solids based on density-functional calculations. *J. Phys. Chem.* **1993**, *97* (33), 8617-8624.
9. Deringer, V. L.; Tchougréeff, A. L.; Dronskowski, R., Crystal orbital Hamilton population (COHP) analysis as projected from plane-wave basis sets. *J. Phys. Chem. A* **2011**, *115* (21), 5461-5466.
10. Maintz, S.; Deringer, V. L.; Tchougréeff, A. L.; Dronskowski, R., Analytic projection from plane-wave and PAW wavefunctions and application to chemical-bonding analysis in solids. *J. Comput. Chem.* **2013**, *34* (29), 2557-2567.
11. Maintz, S.; Deringer, V. L.; Tchougréeff, A. L.; Dronskowski, R., LOBSTER: A tool to extract chemical bonding from plane-wave based DFT. *J. Comput. Chem.* **2016**, *37* (11), 1030-1035.
12. Zhang, H.; Swihart, M. T., Synthesis of tellurium dioxide nanoparticles by spray pyrolysis. *Chem. Mater.* **2007**, *19* (6), 1290-1301.

13. Itoh, Y.; Lenggoro, I. W.; Okuyama, K.; Mädler, L.; Pratsinis, S. E., Size tunable synthesis of highly crystalline BaTiO₃ nanoparticles using salt-assisted spray pyrolysis. *J. Nanopart. Res.* **2003**, 5 (3-4), 191-198.
14. Pennycook, S.; Jesson, D., High-resolution Z-contrast imaging of crystals. *Ultramicroscopy* **1991**, 37 (1-4), 14-38.
15. Bosman, M.; Watanabe, M.; Alexander, D.; Keast, V., Mapping chemical and bonding information using multivariate analysis of electron energy-loss spectrum images. *Ultramicroscopy* **2006**, 106 (11-12), 1024-1032.
16. Varela, M.; Oxley, M. P.; Luo, W.; Tao, J.; Watanabe, M.; Lupini, A. R.; Pantelides, S. T.; Pennycook, S. J., Atomic-resolution imaging of oxidation states in manganites. *Phys. Rev. B* **2009**, 79 (8).
17. Nechache, R.; Harnagea, C.; Li, S.; Cardenas, L.; Huang, W.; Chakrabartty, J.; Rosei, F., Bandgap tuning of multiferroic oxide solar cells. *Nat. Photonics* **2014**, 9 (1), 61-67.
18. Cao, D.; Wang, C.; Zheng, F.; Dong, W.; Fang, L.; Shen, M., High-efficiency ferroelectric-film solar cells with an n-type Cu₂O cathode buffer layer. *Nano Lett.* **2012**, 12 (6), 2803-9.
19. Qin, M.; Yao, K.; Liang, Y. C., High efficient photovoltaics in nanoscaled ferroelectric thin films. *Appl. Phys. Lett.* **2008**, 93 (12), 122904.
20. Gopal Khan, G.; Das, R.; Mukherjee, N.; Mandal, K., Effect of metal doping on highly efficient photovoltaics and switchable photovoltage in bismuth ferrite nanotubes. *Phys. Status Solidi RRL* **2012**, 6 (7), 312-314.
21. Qu, T.; Zhao, Y.; Xie, D.; Shi, J.; Chen, Q.; Ren, T., Resistance switching and white-light photovoltaic effects in BiFeO₃/Nb–SrTiO₃ heterojunctions. *Appl. Phys. Lett.* **2011**, 98 (17), 173507.